Original Article

Institution of MECHANICAL ENGINEERS
Journal of AEROSPACE ENGINEERING

Proc IMechE Part G:
J Aerospace Engineering
2022, Vol. 236(16) 3354–3369

DOI: 10.1177/09544100221083713
journals.sagepub.com/home/pig
SAGE

Linear parameter-varying-based transition flight control design for a tilt-rotor aircraft

Shen Qu, Guoming Zhu, Weihua Su and Sean Shan-Min Swei

Abstract

This paper presents the development of novel transition flight controllers for a class of urban air mobility aircrafts configured with a fixed-wing and six distributed electric rotor assemblies. Only the two tilt-rotors are utilized for thrust vectoring during transition flight from hovering to steady-level flight, while the four lift-rotors are modulated with aerodynamic lift induced by fixed-wing to maintain stable altitude-hold. Three tractable tilt-rotor articulation profiles are proposed by taking into account of various aircraft and hardware constraints. Given a predefined nominal tilting profile, a family of linear models is obtained by linearizing the nonlinear aircraft model at multiple tilt-rotor angular positions along the tilting profile. Using tilt-rotor angular position as a scheduling parameter, a discrete-time linear parameter-varying model can be constructed, which is then used to develop a novel transition flight control architecture that integrates the adaptive model predictive control law with feedforward effect of the dynamic reference compensation. The simulation results demonstrate the effectiveness of proposed transition flight controllers and its robustness subject to external disturbance.

Keywords

Electric vertical takeoff and landing tilting optimization, linear parameter-varying electric vertical takeoff and landing model, model predictive control with dynamic reference compensation, adaptive model predictive control, tilt-rotor aircraft

Date received: 11 July 2021; accepted: 9 February 2022

Introduction

A distributed electric propulsion (DEP) driven urban air mobility (UAM) vehicle concept has proven to be potentially transforming air transportation of the future for intra- and inter-city travel. The key enablers of this disruptive mode of air travel can be attributed to many recent technological advancements on, for instance, power electronics, high-density battery, advanced materials and structures, advanced onboard computing, etc. Still, many technical challenges need to be addressed, as documented comprehensively in Uber Elevate's 2016 White Paper[1]. One of the most promising UAM vehicle platforms considered in recent years is the hybrid eVTOL (electric Vertical Takeoff and Landing) vehicle platform, which combines aerodynamic efficiency of the fixed-wing aircraft with VTOL capability of the multi-rotor DEP system. Some of the highly relevant eVTOL related studies include market prediction for emerging needs[2], route and trajectory planning[3–6] power and energy modeling and optimization,[7–12] vehicle dynamics and control analysis,[13] and failure analysis[14]. Prototypes of many UAM vehicle platforms have already been developed and, in some cases, flight tested, for example, Boeing Swift, Airbus Vahana, Joby S2/S3, Lilium Jet, and Hyundai/Uber S-A1 to just name a few. It is important to highlight that these eVTOL vehicles utilize DEP thrust vectoring capability to enable flight transitioning from hovering to steady-level flight, and vice versa.

The conventional hybrid tilt-rotor aircraft, namely Bell XV-15 and its variant V-22 Osprey, utilizes a pair of rotor-propeller assembly placed at the wingtips, and they are used for VTOL as well as forward flight by articulating the thrust vectors. However, this class of tilt-rotor aircraft is known to be ineffective and unsafe, especially during the transition flight. Many advanced flight control design concepts were proposed aiming to improve the stability, flying qualities, and performance of tilt-rotor aircrafts[15,16].

Department of Mechanical Engineering, Michigan State University, East Lansing, MI, USA
Department of Aerospace Engineering and Mechanics, The University of Alabama, Tuscaloosa, AL, USA
Department of Aerospace Engineering, Khalifa University, Abu Dhabi, United Arab Emirates

Corresponding author:
Guoming Zhu, Department of Mechanical Engineering, Michigan State University, 1497 Engineering Research Court, Room E148, East Lansing, MI 48824, USA.
Email: zhug@egr.msu.edu

In[17,18] the transition flight control of XV-15 was investigated using model predictive control (MPC) and time-varying linear control, respectively, and in[19] an adaptive model inversion control was used to improve the closed-loop performance and also to reduce the control development cycle. Contrary to the conventional tilt-rotor aircraft, the DEP enabled hybrid eVTOL vehicles offer much more operational stability and agility, allowing for a higher degree of fault tolerance and robustness. However, the aerodynamic complexity of transition flight from hovering to level flight, and the flight control design for stable transition, is still a challenging subject of research.

The development of the tractable tilt-rotor articulation profile for hybrid eVTOL vehicles is also an open question. Given the vehicle specifications and operational constraints including the flying qualities and passenger ride quality, the goal of articulation profile design is to develop a tilting trajectory that is best suited for the type of aircraft at its given flight conditions. In[20], the tilting trajectory was optimized for a quadrotor aircraft using the ant colony optimization algorithm, and in[21], the takeoff trajectory of a tilt-rotor aircraft was optimized using the direct allocation method. In[22,23] the dynamic modeling and control of a hybrid eVTOL vehicle configured with four synchronized tilt-rotors were considered. There are other eVTOL vehicles that utilize a DEP system with various number of lift-rotors and tilt-rotors. For example, Joby S4 and Uber eCRM-001 are both configured with six rotors, but Joby S4 has only two tilt-rotors for synchronous articulation, whereas in eCRM-001, all six rotors can be articulated. Another DEP enabled high technology readiness level (TRL) hybrid eVTOL vehicle is Solvay VA-1X, and it features four tilt-rotors and four lift-rotors, separately.

In this paper, a hybrid eVTOL aircraft configured with six distributed rotors is considered in[24], in which two pairs of lift-rotors are placed at fore and aft of the aircraft center of gravity (CG), and one pair of tilt-rotors at the wingtips, closer to CG in the longitudinal direction, is commanded to articulate synchronously. We present the studies of three tilt-rotor articulation profiles for transition flight subject to hardware constraints and flying/ride quality specifications. In particular, by leveraging the distributed rotors for reconfigurable thrust vectoring, more aggressive and optimal tilting profiles can be developed in which the optimal profile is the one that consumes the minimum total propulsion energy. A control-centric LPV (linear parameter-varying) model[25–27] is developed to characterize the aircraft flight transition process along a prescribed articulation profile. Through linearization of nonlinear aircraft model with respect to a set of equilibrium flight conditions, a set of linear time-invariant models can be attained.[28,29] However, such a modeling approach leads to a large modeling error because of the presence of nonzero longitudinal vehicle acceleration during the transition flight. In order to reduce the LPV modeling error, a trajectory linearization method is adopted in this study; hence, a set of discretized and linearized models can be obtained through trajectory linearization along the tilting profile; furthermore, these discrete-time linearized models are then used to construct the LPV aircraft transition flight model. The adaptive MPC method[30–33] is used for designing the transition flight controllers based on the developed LPV model.[34–36] Note that the MPC utilizes a specific set of penalty weightings to shape the target output performance. In this paper, in order to improve the closed-loop system performance and reduce the real-time computational cost, two critical modifications are introduced to the proposed adaptive MPC law, namely integration of feedforward control via dynamic reference compensation (DRC) and utilization of event-driven/time-varying weightings and hard constraints. Finally, the performance of the proposed adaptive MPC-DRC strategy is evaluated in Matlab/Simulink environment using the nonlinear rigid-body eVTOL model[24]. Additional simulations are conducted to demonstrate the disturbance rejection performance of the proposed adaptive MPC-DRC transition flight controllers. Note that the flying qualities and passenger ride quality were considered during the transition profile and control design and validated in simulations. For example, during the transition optimization, the flying and ride qualities were considered by setting the tilt-transition period, maximum acceleration, and rotor thrust limits; and during control design, these were considered by using MPC-DRC with hard constraint on rotor thrust to minimize the tilt-transition tracking error.

The main contribution of the paper is three-fold. First, a tilt-rotor aircraft transition energy optimization method is proposed based on an aircraft force balance model, using the trapezoidal quadrature rules for solving the optimal trajectory. Second, a control-oriented LPV model has been constructed by linearizing the nonlinear aircraft model along the transition trajectory, which reduced the modeling error compared to the steady-state LTI model based LPV modeling method. Lastly, an adaptive MPC design framework with control input constraints and dynamic reference compensation (MPC-DRC) is proposed for studying transition control under normal and disturbed tilt-transition conditions, where the control performance is validated through simulation study based on the nonlinear aircraft model.

This paper is organized as follows. The section Nonlinear Flight Dynamic Model of Tilt-Rotor Aircraft reviews the nonlinear rigid-body dynamics of the hybrid eVTOL UAM aircraft, followed by the tilt-rotor transition planning and trajectory optimization in the section Reference Articulation Trajectory for Tilt-Rotors. The section Linear Parameter-varying Modeling of Transition Flight presents the development of a control-centric LPV model for transition flight, based on a collection of linearized models along the prescribed tilting trajectory. The section Adaptive MPC-DRC for LPV Systems provides a detailed assessment of the adaptive MPC-DRC design subjected to time-varying weightings and hard constraints, and the simulation results are presented in the section Simulation Results to validate the proposed transition flight control concepts. Concluding remarks are summarized in the final section.

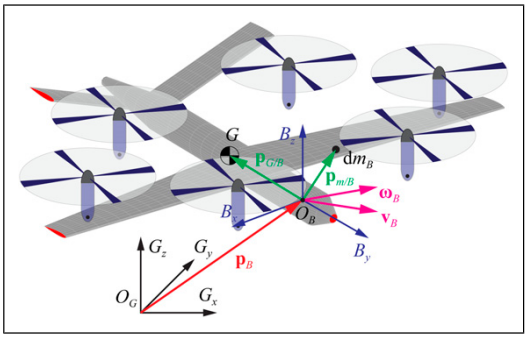

Figure 1. Global and body reference frames of a rigid-body tilt-rotor aircraft (connections between rotors and aircraft are not shown).

Table 1. Inertial properties of urban air mobility (UAM) aircraft.

	Value	Unit
Body mass, m_B	2240.73	kg
Body moment of inertia, $\mathbf{I}_{B,xx}$	12 000	kg m^2
Body moment of inertia, $\mathbf{I}_{B,yy}$	9400	kg m^2
Body moment of inertia, $\mathbf{I}_{B,zz}$	20 000	kg m^2
Rotor mass, m_r	4.55	kg
Rotor moment of inertia $\mathbf{I}^e_{r,xx}$	3.5	kg m^2
Rotor moment of inertia $\mathbf{I}^e_{r,yy}$	7.0	kg m^2
Rotor moment of inertia $\mathbf{I}^e_{r,zz}$	3.5	kg m^2

Nonlinear flight dynamic model of tilt-rotor aircraft

Figure 1 illustrates an aircraft configured with a fixed-wing planform with several tilt-rotors, and its inertial properties are stated in Table 1. As being discussed in[24], the dynamic contributions of fixed-wing aircraft and tilt-rotors are modeled separately and combined for the full aircraft study. First, a body-fixed frame B is defined with respect to the inertial frame G to describe the aircraft's position and orientation with B_x pointing to the right wing, B_y pointing forward, and B_z completing the right-hand rule. While the B frame can be arbitrarily placed, it is convenient to set the frame's origin O_B within the aircraft's symmetric plane. The inertial position of O_B is represented by $\mathbf{p}_B$, while $\mathbf{p}_{G/B}$ describes the position of the mass center of the fixed-wing aircraft (excluding the tilt-rotors) with respect to the B frame. The aircraft's rigid-body velocity is given by

$$\boldsymbol{\beta} = \begin{Bmatrix} \mathbf{v}_B \\ \boldsymbol{\omega}_B \end{Bmatrix} = \begin{Bmatrix} \dot{\mathbf{p}}_B + \boldsymbol{\omega}_B \times \mathbf{p}_B \\ \dot{\boldsymbol{\theta}}_B \end{Bmatrix} \tag{1}$$

where $\mathbf{v}_B$ and $\boldsymbol{\omega}_B$ denote the translational and angular velocities of the rigid-body, respectively. Note that all the kinematic quantities are resolved in the B frame.

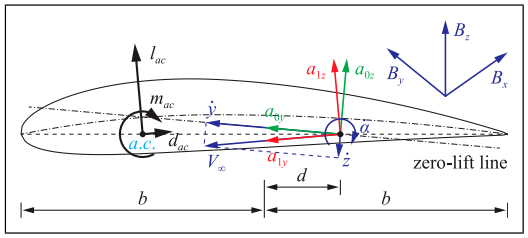

Figure 2. Aerodynamic frame and load components.

By following the Hamilton's principle, the flight dynamic equation of motion of the tilt-rotor is found as[24]

$$\mathbf{M}_{BB}(\rho)\dot{\boldsymbol{\beta}} + \mathrm{C}_{BB}(\boldsymbol{\beta},\rho)\boldsymbol{\beta} = \mathbf{R}_B \tag{2}$$

where ρ denotes the tilt angles of all rotors. The inertia matrix $\mathbf{M}_{BB}(\rho)$, damping matrix $\mathbf{C}_{BB}(\boldsymbol{\beta},\rho)$, and load vector $\mathbf{R}_B$ are given by

$$\begin{aligned}
\mathbf{M}_{BB} &= \begin{bmatrix} m_B\mathbf{I}_3 & m_B\tilde{\mathbf{p}}^T_{\frac{G}{B}} \\ m_B\tilde{\mathbf{p}}_{\frac{G}{B}} & \mathbf{I}_B \end{bmatrix} + \begin{bmatrix} m_r\mathbf{I}_3 & m_r\tilde{\mathbf{p}}^T_{\frac{A}{B}} \\ m_r\tilde{\mathbf{p}}_{\frac{A}{B}} & \mathbf{I}_r + m_r\tilde{\mathbf{p}}_{\frac{A}{B}}\tilde{\mathbf{p}}^T_{\frac{A}{B}} \end{bmatrix} \\
\mathrm{C}_{BB} &= \begin{bmatrix} m_B\tilde{\boldsymbol{\omega}}_B & m_B\tilde{\boldsymbol{\omega}}_B\tilde{\mathbf{p}}^T_{\frac{G}{B}} \\ m_B\tilde{\mathbf{p}}_{\frac{G}{B}}\tilde{\boldsymbol{\omega}}_B & \tilde{\boldsymbol{\omega}}_B\mathbf{I}_B \end{bmatrix} \\
&\quad + \begin{bmatrix} m_r\tilde{\boldsymbol{\omega}}_B & m_r\tilde{\boldsymbol{\omega}}_B\tilde{\mathbf{p}}^T_{\frac{A}{B}} \\ m_r\tilde{\mathbf{p}}_{\frac{A}{B}}\tilde{\boldsymbol{\omega}}_B & \tilde{\omega}_B\mathbf{I}_r + m_r\tilde{\mathbf{p}}_{\frac{A}{B}}\tilde{\boldsymbol{\omega}}_B\tilde{\mathbf{p}}^T_{\frac{A}{B}} \end{bmatrix} \\
\mathbf{R}_B &= \mathbf{R}^{\mathrm{grav}} + \mathbf{R}^{\mathrm{iner}} + \mathbf{R}^{\mathrm{rate}} + \mathbf{R}^{\mathrm{gyro}} + \mathbf{R}^{\mathrm{ext}}
\end{aligned} \tag{3}$$

where $\mathbf{I}_3$ is a 3-by-3 identity matrix. m_B, M_r, $\mathbf{I_B}$, and $\mathbf{I_r}$ are the inertia properties listed in Table 1 $\mathbf{p}_{A/B}$ are the position of the mass center of each tilt-rotors, relative to the $\mathbf{B}$ frame. The operator $[\tilde{\cdot}]$ refers to a skew symmetric matrix to complete the cross product of two vectors, that is, $\mathbf{a}\times\mathbf{b} = [\tilde{\mathbf{a}}]\{\mathbf{b}\} = [\tilde{\mathbf{b}}]^T\{\mathbf{a}\}$. $\mathbf{R}_B$ is the external load that includes gravity, gyroscopic, propulsive, and aerodynamic loads. It is worth mentioning that the aerodynamic load is first calculated at each section along the span of lifting surfaces. By doing so, the lifting surfaces are meshed with 1-D elements along their span. See[24] for details.

Refer to Figure 2 for airfoil velocity components, which are decomposed within a local aerodynamic frame a_0, determined by the zero lift line. The 2-D quasi-steady aerodynamic loads on each thin airfoil section undergoing arbitrary motions in an incompressible inviscid subsonic flow are described by

$$\begin{aligned}
l_{ac} &= \pi\rho b^2\left(-\ddot{z} + \dot{y}\dot{\alpha} - d\ddot{\alpha}\right) + 2\pi\rho b\dot{y}^2\left[-\frac{\dot{z}}{\dot{y}} + \left(\frac{1}{2}b - d\right)\frac{\dot{\alpha}}{\dot{y}}\right] \\
&\quad + \rho b\dot{y}^2 c_{l\delta}\delta \\
m_{ac} &= \pi\rho b^3\left[\frac{1}{2}\ddot{z} - \dot{y}\dot{\alpha} - \left(\frac{1}{8}b - \frac{1}{2}d\right)\ddot{\alpha}\right] + 2\rho b^2\dot{y}^2 c_{m\delta}\delta
\end{aligned}$$

$$d_{ac} = -2\pi\rho b\dot{y}^2\left(-\frac{\dot{z}}{\dot{y}} - d\frac{\dot{\alpha}}{\dot{y}}\right)^2 + \rho b\dot{y}^2 c_{d\delta}\delta \tag{4}$$

where δ is the trailing-edge flap deflection angle, b is the semichord, and d is the distance of midchord in front of the reference axis. The sectional aerodynamic loads are transformed from the a_1 frame to the body frame B which is given by

$$\begin{aligned}\mathbf{f}^{\text{aero}} &= \mathbf{C}^{Ba_1}\{0 \quad d_{ac} \quad l_{ac}\}^T \\ \mathbf{m}^{\text{aero}} &= \mathbf{C}^{Ba_1}\left\{m_{ac} + l_{ac}\left(\frac{1}{2}b + d\right) \quad 0 \quad 0\right\}^T\end{aligned} \tag{5}$$

The distributed aerodynamic force and moment are further integrated to obtain the resultant aerodynamic load about the B frame as follows

$$\mathbf{R}^{\text{aero}} = \begin{Bmatrix}\mathbf{E}_f\mathbf{f}^{\text{aero}} \\ \mathbf{E}_m\mathbf{m}^{\text{aero}}\end{Bmatrix} \tag{6}$$

where $\mathbf{E}_f$ and $\mathbf{E}_m$ are the influence matrices determined by the numerical integration scheme. Eventually, $\mathbf{R}^{\text{aero}}$ contributors to the external loads shown in equation (3).

The aerodynamic calculation applied herein does not consider the wing-body combination. According to Anderson,[37] in a subsonic flow, the lift that is generated on a fuselage is approximately the same as the one that is created by the wing area masked by the fuselage. In the current work, the wing planform area includes the portion that is masked by the body, as shown in Figure 3). On the other hand, the drag created by the fuselage is not included. Such drag mainly comes from the interference drag and friction drag, which do not change with the lift. Further consideration of the aerodynamic coupling among the wing, fuselage, and propellers will involve a comprehensive model. As the purpose of the current work is to explore a robust control algorithm for the class of urban air mobility vehicles, the simplified model neglecting such drag components can provide an effective estimation of the aerodynamic loads for the control development, while not impacting the qualitative answers.

For control design purpose, the nonlinear aircraft model is linearized with respect to a prescribed operational trajectory so as to render an LPV state-space model that is best suited for control design. To facilitate the presentation, the system states, inputs, and outputs are as defined in Table 2.

Reference articulation trajectory for tilt-rotors

For tilt-rotor aircraft, a stable transition from hover to level flight demands a well-orchestrated flight control strategy, and this is especially critical for vehicles that feature a combination of fixed-wing and distributed electric propulsion. As shown in Figure 3, only the two middle rotors are designated to articulate for thrust vectoring to support both vertical and forward flights. A high-level concept of operation for transition flight is illustrated in Figure 4. It is assumed that, during the transition flight, aircraft is maintained at certain designated altitude and is subjected to attitude-hold and zero vertical and lateral velocity. Therefore, at the beginning of transition, in order to gain forward velocity, the middle two tilt-rotor thrust vectors are articulated by following a prescribed tilt trajectory, while satisfying specific constraints. As aircraft picks up forward velocity, the fixed-wing aerodynamic effect starts to emerge, in which the wing-induced lift force increases gradually; as a result, the front and rear lift-rotor thrusts can be correspondingly tuned down by reducing their spin rates. At the end of transition, the front and rear lift-rotor thrusts reduce to zero, the two tilt-rotors are completely transformed to become push rotors, and the aircraft now flies as a twin propeller-driven fixed-wing aircraft.

To optimize the transition flight performance from hover to level flight, a tracking control problem is formulated for the middle two tilt-rotors to follow a reference tilt trajectory by modulating the tilt angle and aircraft forward velocity. As a result, the optimal tilt trajectory that minimizes the total control energy during transition flight can be attained.

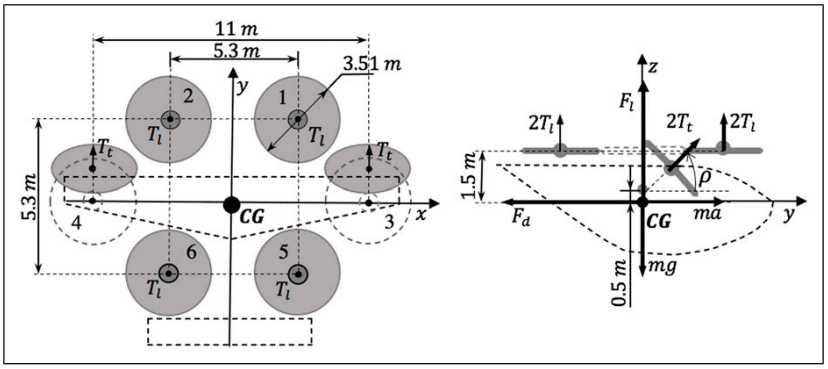

Figure 3. Geometry of urban air mobility (UAM) aircraft with dynamic force analysis.

Table 2. System input and output definition.

System Input	Order	System state	Order
Front right/left rotor spin acceleration	u_1/u_2	Rigid-body velocity	x_1 to x_6
Mid right/left rotor spin acceleration	u_3/u_4	Euler angle	x_7 to x_9
Rear right/left rotor spin acceleration	u_5/u_6	Body inertial position	x_{10} to x_{12}
Ruddervator deflection	u_7	Propeller speed	x_{13} to x_{18}
Mid right/left rotor tilt acceleration	u_8/u_9	Mid right/left rotor tilt angle	x_{19} to x_{20}
—	—	Mid right/left rotor tilt rate	x_{21} to x_{22}
System output	Order	System output	Order
Lateral speed in body frame	y_1	Roll angle (θ_y)	y_7
Longitudinal speed in body frame	y_2	Pitch angle (θ_x)	y_8
Vertical speed in body frame	y_3	Yaw angle ($-\theta_z$)	y_9
Pitch rate ($\dot{\theta}_x$)	y_4	Lateral displacement (D_x)	y_{10}
Roll rate ($\dot{\theta}_y$)	y_5	Longitudinal displacement (D_y)	y_{11}
Yaw rate ($\dot{\theta}_z$)	y_6	Vertical displacement (D_z)	y_{12}
Mid right/left rotor tilt angle	$y_{13/14}$	Mid right/left rotor tilt rate	$y_{15/16}$

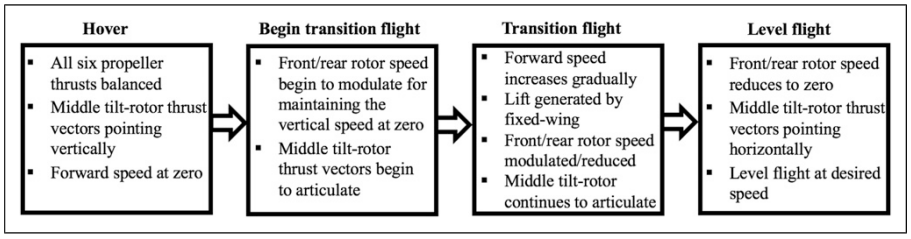

Figure 4. Concept of operation for transition flight.

A simplified aircraft model

Since the aircraft is under attitude-hold and allows only the longitudinal directional motion during transition, a 2-D force equation can be derived by referring to Figure 3. Following the standard notions of fixed-wing aircraft, the total drag F_d and lift F_l are with respect to the aircraft CG (center of gravity), each of the lift-rotor at front and rear generates the same synchronized thrust T_l, and each of the middle tilt-rotor produces the thrust T_t. Note that the pivot point of T_t is 0.5 m above the CG, meaning that the thrust vector T_t will deviate slightly from the aircraft CG in the longitudinal direction when the rotor starts to tilt, and for simplification, this small deviation is omitted from the tilt trajectory optimization process. Also, for constructing a feasible optimization problem in the designed scope of this project, the aircraft pitch motion is assumed to be held at zero during the transition trajectory optimization process, and the 2-D force balancing equations can be given by

$$\begin{cases} F_l + 4T_l + 2\sin(\rho)T_t = mg \\ 2\cos(\rho)T_t - F_d = ma \end{cases} \tag{7}$$

where $\rho \in [90,\ 0] -$ deg denotes the tilt-rotor angular position and a the longitudinal acceleration, and the lift, drag, and rotor thrusts are defined as

$$\begin{cases} F_l = \frac{1}{2}C_l\rho_a A V_y^2,\ F_d = \frac{1}{2}C_d\rho_a A V_y^2 \\ T_t = C_t\rho_a n_t^2 D^4, T_l = C_t\rho_a n_l^2 D^4 \end{cases} \tag{8}$$

Note that C_l and C_d are the lift and drag coefficients, C_t is the thrust coefficient, ρ_a is the air density, A is the wing area, and V_y is the forward velocity. In addition, n_l and n_t denote the lift-rotor and tilt-rotor speed, and D is the rotor diameter.

At the beginning of transition flight, the aerodynamic lift force $F_l = 0$ and the tilt angle $\rho = 90$-deg; hence, the aircraft weight mg is balanced by the vertical thrusts $4T_l + 2T_t$. As tilt-rotors start to articulate, the forward velocity V_y and acceleration a increases, so do F_l and F_d; therefore, T_l can be gradually reduced according to F_l so as to balance the aircraft weight. At the end of transition, $\rho = 0$-deg and $T_l = 0$, the aircraft reaches a steady-level flight, that is, $F_l = mg$, at the desired cruising speed.

Transition flight profiles

The goal of the transition flight profile study for hybrid eVTOL vehicles is to develop tractable vehicle transition flight path and associated tilt-rotor articulation profiles, so as to warrant a stable transitioning from hovering to steady-level flight, when subjected to vehicle performance

and hardware constraints, such as allowable peak rotor thrust, aircraft flying qualities, and passenger ride quality. In this study, three cases of transition flight profiles are considered with respect to a scheduled transition timeline of $[t_0, t_1, t_2, t_3]$. This timeline is formulated according to the planned vehicle longitudinal acceleration and velocity. That is, from t_0 to t_1, the aircraft longitudinal acceleration is to change from 0 to the maximum acceleration $a_{\max}$; from t_1 to t_2, the acceleration is to maintain at $a_{\max}$; and finally, from t_2 to t_3, the acceleration is to reduce down to zero. Based on the passenger ride-comfort specification, the maximum allowable vehicle longitudinal acceleration $a_{\max}$ is constrained by 0.189 g ,[38] where $g = 9.8\ m/s^2$ is the gravitational acceleration. In addition, the maximum rotor rotational speed N_p is 1146 r/min, which yields the maximum rotor thrust level T_{t1}, and the maximum designated tilt-rotor articulation rate $\dot{\rho}_{\max}$ is chosen to be 9 deg/s. In what follows, we study the three transition flight profiles.

As a baseline study, Case 1 presents an ordinary tilt-rotor articulation profile, featuring an initial ramping-up period, followed by cruising at constant tilt-rate, and final winding down to complete the transition flight. More specifically, from 0 to 1s, the tilt-rotor articulation is to linearly accelerate and reach the targeted tilt-rate of 2 deg/s; from 1s to 45 s, the tilt-rate is to coast at 2 deg/s; and finally, from 45 to 46 s, the tilt-rate is to reduce linearly to zero. A simple calculation over this profile confirms that the total angular distance traveled is 90-deg. At the beginning of transition flight t_0, the tilt-rotor rotational speeds are held at a predetermined maximum speed N_p, and as tilt-rotors begin to articulate, the aircraft starts to accelerate and pick up forward velocity; hence, the longitudinal acceleration reaches the maximum allowable $a_{\max}$ at t_1. From t_1 to t_2, the tilt-rotor thrusts are regulated so as to maintain the longitudinal acceleration at $a_{\max}$, while the aircraft continues to gain forward velocity. As a result, the aerodynamic lift force induced by fixed-wing emerges, and correspondingly, the four lift-rotor thrust levels can be tailored to maintain altitude-hold. From t_2 to t_3, the longitudinal acceleration is to reduce from $a_{\max}$ to zero by adjusting the tilt-rotor thrust level, and the aircraft is to reach or continue the desired level flight velocity V_c.

The targeted coasting tilt-rate of 2 deg/s in Case 1 is chosen based on the previous study conducted for a twin tilt-rotor aircraft XV-15.[17] However, with the proposed distributed electric propulsion platform, a higher tilt-rate can be commanded without compromising the vehicle stability during transition flight. The primary goal of rapid tilt-rotor maneuver is to develop vehicle forward velocity as soon as possible; hence, the aerodynamic lift can be generated much sooner so as to save the total energy. Therefore, in Case 2, we propose an aggressive tilt-rotor articulation profile aiming for the aircraft to quickly reach the maximum longitudinal acceleration $a_{\max}$ at t_1 by commanding maximum tilt-rate $\dot{\rho}_{\max}$ and maximum thrust level T_{t1}. At t_1, the corresponding vehicle forward velocity $V_y(t_1) = V_{y1}$. Specifically, from t_1 to t_3, the vehicle reference acceleration and velocity profiles are proposed as follows

$$a(t) = \begin{cases} a_{\max} & \forall t \in [t_1, t_2] \\ a_{\max}\dfrac{t_3 - t}{t_3 - t_2} & \forall t \in [t_2, t_3] \end{cases} \tag{9}$$

$$V_y(t) = V_{y1} + \int_{t_1}^{t_3} a(t)dt,\ \text{s.t.} V_y(t_1) = V_{y1},\ V_y(t_3) = V_c \tag{10}$$

where $a_{\max}$, V_c, V_{y1}, and t_1 are known, and t_2, t_3 can be calculated, respectively, based on the predefined level flight convergence duration t_s, where $t_s = t_3 - t_2$. In this case, t_s is chosen to be 5 s, t_1 and t_2 are calculated as 3.215 and 36.58 s, respectively, hence $t_3 = 41.58\ s$. Apparently, the proposed aggressive tilt-rotor articulation profile can indeed expedite the transition flight when compared to the baseline profile.

In Case 3, we consider the same scheduled timeline as in Case 2, but propose an optimal articulation profile that consumes minimum energy. In particular, from t_1 to t_3, the total energy E and the instant power $P(t)$ of all six rotors can be given by

$$E = \int_{t_1}^{t_3} P(t)dt,\ P(t) = 4C_p\rho_a n_l(t)^3 D^5 + 2C_p\rho_a n_t(t)^3 D^5 \tag{11}$$

where C_p denotes the power coefficient, $n_l(t)$ and $n_t(t)$ are the lift- and tilt-rotor rotational speeds derived from equations (7) and (8) as

$$\begin{cases} n_t(t) &= \left[\dfrac{ma(t) + \frac{1}{2}C_d\rho_a A V_y(t)^2}{2C_t\rho_a D^4 \cos(\rho(t))}\right]^{\frac{1}{2}} \\ n_l(t) &= \left[\dfrac{mg - 2\sin(\rho(t))C_t\rho_a n_t(t)^2 D^4 - \frac{1}{2}C_l\rho_a A V_y(t)^2}{4C_l\rho_a D^4}\right]^{\frac{1}{2}} \end{cases} \tag{12}$$

Note that $a(t)$ and $V_y(t)$ are known. By substituting $n_l(t)$ and $n_t(t)$ into equation (12), the problem of energy

Table 3. Aircraft parameters.

Parameter	Value	Parameter	Value	Parameter	Value
C_l	0.3141	C_d	0.0166	C_p	8.4×10^{-5}
C_t	5.6×10^{-4}	ρ_a, kg/m^3	1.225	A, m^2	25
D, m	3.51	a_{max}, m/s^2	1.85	$\dot{\rho}_{max}$, deg/s	9
t_s, s	5	N_p, rpm	1146	g, m/s^2	9.81

minimization is now converted into finding $\rho(t)$ that minimizes the total energy cost E, that is

$$\min E = \min_{\rho(t)} \int_{t_1}^{t_3} P(t)dt = \min_{\rho(t)} \int_{t_1}^{t_3} \left[4C_p\rho_a n_l(t)^3 D^5 + 2C_p\rho_a n_t(t)^3 D^5\right] dt \tag{13}$$

It is difficult to directly solve the optimization problem as presented in the form of equation (13). Thus, we propose that the integral in equation (13) be approximated using trapezoidal quadrature rule by dividing integration horizon $[t_1, t_3]$ into N_d sections with a step size of $\delta = (t_3 - t_1)/N_d$, that is

$$\int_{t_1}^{t_3} P(t)dt \approx \sum_{k=0}^{N_d-1} \frac{\delta}{2}(P(k) + P(k+1)) \tag{14}$$

and this approximation is accurate if N_d is chosen to be sufficiently large. We assume that the tilt angle $\rho \in [\rho_i, \rho_{i+1}]$ can be linearly interpolated between the two sample points, ρ_i and ρ_{i+1}. Note that $P_k = P(k) \geq 0$ is a constrained nonlinear function of $\rho_k = \rho(k)$ defined by equations (13) and (14). Hence, the optimal tilt angle ρ_k ($k = 0, 1, \ldots, N_d - 1$) can be obtained by solving the following optimization problem

$$\min_{\rho_k} P_k(\rho_k) \text{for } k = 0, 1, \ldots, N_d - 1 \tag{15}$$

By substituting relevant aircraft parameters given in Table 3 into equation (15), the optimal tilt-rotor articulation profile from t_1 to t_3 can be attained by solving $dP_k/d\rho_k = 0$ ($k = 0, 1, \ldots, N_d - 1$).

Figure 5 shows the reference aircraft forward velocity $V_y(t)$, the tilt-rotor articulation profile $\rho(t)$, and the tilt-rotor rotational speed $n_t(t)$ for the three cases described above. They all have successfully transitioned to the desired level flight velocity within the specified duration; however, the total energy cost for Case 1 is 3.05 kWh, for Case 2 is 2.64 kWh, and for Case 3 is 2.56 kWh. This further proves the advantage of the proposed minimum energy reference profile.

Linear parameter-varying modeling of transition flight

This section presents an LPV model that captures the transition flight dynamics as the two tilt-rotor thrust vectors articulate from vertical to horizontal.

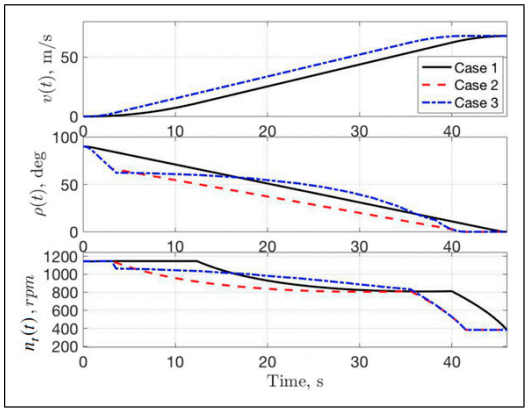

Figure 5. Comparison of three reference trajectories during transition flight.

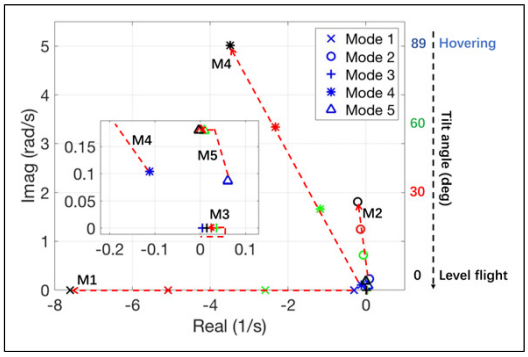

Figure 6. Root loci during transition.

Steady-state dynamics analyzation

First, the steady-state dynamics of aircraft is investigated at the trimmed points along the transition, and the stability modes at each stage are showed in Figure 6,where blue, green, red, and black colors represent these poles associated with tilt angles of 89, 60, 30, and 0 degree, respectively. Noting that the first stage of tilt angle is defined at 89°, instead of 90°, so that the aircraft dynamic modes can be found under tilt transition. Note that dynamic modes under hovering are different from these under tilt transition. Pole locations of five dominant aircraft modes are plotted and denoted by Modes 1 to 5 using "×," "o," " + ," "*," and "△," respectively, and associated mode physical meaning and values are summarized in Table 4. Note that modes 2, 4, and 5 are

Table 4. Information of aircraft modes.

Mode ID	Rigid-body mode	89deg 1 m/s	60-deg 22.7 m/s
1	Rolling	−0.300 8	−2.585 5
2	Dutch roll	0.0892 ± 0.2 293i	−0.058 7 ± 0.7 145i
—	ω_n	0.246	0.716 9
—	ζ	−0.362 5	0.081 9
3	Spiral	0.004 9	0.036 2
4	Short period	−0.111 7 ± 0.1 043i	−1.169 6 ± 1.6 673i
—	ω_n	0.152 8	2.036 6
—	ζ	0.730 9	0.574 3
5	Phugoid	0.060 5 ± 0.087i	0.008 8 ± 0.18i
—	ω_n	0.106	0.180 2
—	ζ	−0.570 9	−0.048 8
Mode ID	Rigid-body mode	30-deg 45.3 m/s	0-deg 68 m/s
1	Rolling	−5.080 9	−7.600 5
2	Dutch roll	−0.139 6 ± 1.248i	−0.207 1 ± 1.8 156i
—	ω_n	1.255 8	1.827 4
—	ζ	0.111 2	0.113 3
3	Spiral	0.024 0	0.014 7
4	Short period	−2.323 9 ± 3.3 413i	−3.481 4 ± 5.0 149i
—	ω_n	4.07	6.104 9
—	ζ	0.571	0.570 3
5	Phugoid	0.001 1 ± 0.1 803i	−0.003 ± 0.1 804i
—	ω_n	0.180 4	0.180 4
—	ζ	−0.006 1	0.016 6

complex, and their natural frequencies ω_n and damping ratio ζ_n ($n = 2, 4, 5$) can be calculated based on equation (16) below

$$\omega_n = \sqrt{Re(\lambda_n)^2 + \mathrm{Im}(\lambda_n)^2},\ \zeta_n = \frac{Re(\lambda_n)}{\omega_n} \tag{16}$$

where $Re(\lambda_n)$ and $Im(\lambda_n)$ denote the real and imaginary parts of the n^{th} eigenvalue, respectively. By looking into natural frequencies and damping ratios, the aircraft oscillation frequencies and decay rates can be obtained. The rolling and short period modes (#1 and #4) remain stable during the entire tilt-transition process with increasing natural frequencies. The Dutch roll mode (#2) varies from unstable to stable with increased damping ratio, which is benefited from the increased fixed-wing aerodynamic lift. As for the phugoid mode (#5), it finally becomes stable when the aircraft achieves level flight (cruising) condition. Last but not the least, note that the spiral mode (#3) is always slow and unstable, which is a common characteristic of aircraft. It means that a small roll angle change caused by external disturbance could slowly diverge the vehicle rolling angle, yaw angle, and altitude, leading to a spiral flight trajectory towards the ground.

Linearization along a nominal trajectory

Consider a nonlinear aircraft model in the state-space form described by

$$\dot{x}(t) = f(x(t), u(t)) \tag{17}$$

where f is a differentiable function of state $x(t) \in \mathbb{R}^{n_x}$ and control input $u(t) \in \mathbb{R}^{n_u}$. We assume that $x(t) = x_0(t) + \Delta x(t)$ and $u(t) = u_0(t) + \Delta u(t)$, where pair $x_0(t)$ and $u_0(t)$ denote the nominal state and control, respectively, and pair $\Delta x(t)$ and $\Delta u(t)$ denote small deviations from the nominal condition. In addition, pair $x_0(t)$ and $u_0(t)$ satisfy

$$\dot{x}_0(t) = f(x_0(t), u_0(t)) \tag{18}$$

Therefore, equation (17) can be rewritten as

$$\dot{x}_0(t) + \Delta\dot{x}(t) = f(x_0(t) + \Delta x(t), u_0(t) + \Delta u(t)) \tag{19}$$

By applying the Taylor series expansion to the above, we obtain

$$\begin{aligned}\dot{x}_0(t) + \Delta\dot{x}(t) = {} & f(x_0(t), u_0(t)) + \mathcal{A}\Delta x(t) + \mathcal{B}\Delta u(t) \\ & + \boldsymbol{\Psi}_f\Big(\Delta x(t), \Delta\dot{x}(t), \Delta u(t)\Big)\end{aligned} \tag{20}$$

where $\mathcal{A}$ and $\mathcal{B}$ represent the sensitivity matrices at the given nominal condition, and Ψ_f denotes the collection of higher order terms that are negligible. Substituting equation (18) into equation (20) yields

$$\Delta\dot{x}(t) = \mathcal{A}\Delta x(t) + \mathcal{B}\Delta u(t) \tag{21}$$

Since $\Delta\dot{x}(t) = \dot{x}(t) - \dot{x}_0(t)$, equation (21) can be rewritten as below, assuming that the system output $y(t)$ is a linear function of system states

$$\begin{cases} \dot{x}(t) & = \dot{x}_0(t) + \mathcal{A}\Delta x(t) + \mathcal{B}\Delta u(t) \\ y(t) & = Cx(t) \end{cases} \tag{22}$$

which can be converted into the discrete-time form with a sampling period T as

$$\begin{cases} x(k+1) - x_0(k+1) = \dot{x}_0(k)T + A\Delta x(k) + B\Delta u(k) \\ y(k) = Cx(k),\ k = 0, 1, \ldots \end{cases} \tag{23}$$

where (A, B) are the discrete-time system matrices derived from $(\mathcal{A}$,B), and $x_0(k)$ and $\dot{x}_0(k)$ represent the nominal state and its derivative at k.

Affine LPV model for nominal trajectory

An LPV model can be developed by linearly interpolating the state-space models at two adjacent operational conditions along the nominal trajectory over a varying parameter (or scheduling parameter).[39] We assume that the tilt-rotor angular position $\rho(t)$ is measurable in real-time. Consider a family of M linearized system models obtained along the given nominal tilting trajectory, which covers from the start to the end of tilting sequence with ρ as the scheduling parameter. This family of linear models can be defined as

$$\begin{cases} x(k+1)x_0^i(k+1) + \dot{x}_0^i(k)T + A^i\Delta x(k) + B^i\Delta u(k) \\ y(k) = Cx(k) \end{cases} \tag{24}$$

where $i = 1, 2, \ldots, M$ denotes the i-th linearized model at ρ^i. Therefore, the discrete-time affine LPV model can be formulated as follows

$$\begin{cases} x(k+1) = x_0(\rho(k+1)) + \dot{x}_0(\rho(k))T + A(\rho(k))\Delta x(k) \\ + B(\rho(k))\Delta u(k) y(k) = Cx(k) \end{cases} \tag{25}$$

where $\Delta x(k) = x(k) - x_0(\rho(k))$ and $\Delta u(k) = u(k) - u_0(\rho(k))$, and the system matrices $A(\rho(k))$ and $B(\rho(k))$ are given by

$$\begin{aligned} A(\rho(k)) &= A^i + \left(A^{i+1} - A^i\right)\frac{\rho(k) - \rho^i}{\rho^{i+1} - \rho^i}, \\ \rho(k) &\in \left[\rho^i, \rho^{i+1}\right], i = 1, 2, \ldots, M-1 \\ B(\rho(k)) &= B^i + \left(B^{i+1} - B^i\right)\frac{\rho(k) - \rho^i}{\rho^{i+1} - \rho^i}, \\ \rho(k) &\in \left[\rho^i, \rho^{i+1}\right], i = 1, 2, \ldots, M-1 \end{aligned} \tag{26}$$

It should be noted that $\rho(k+1)$ in equation (25) cannot be measured at time step k; however, if the sampling rate is chosen to be sufficiently high, then the difference between the two time steps is negligible; hence, we can assume that $\rho(k+1) \approx \rho(k)$ when T is very small. Therefore, the resulting LPV model approximates the nonlinear aircraft dynamics along the desired operational trajectory as a function of $\rho(k)$ in which the sampling period T is chosen to be 1 *msec*. The following list summarizes steps of the LPV modeling process.

(1) Define the aircraft transition trajectory in terms of $\rho(t)$, $V_y(t)$, and $a(t)$ over the transition flight period $[t_0, t_3]$, based on the approaches specified in the Section Reference Articulation Trajectory for Tilt-Rotors.
(2) Define the number (M) of LTI models to be linearized along the tilting trajectory and select the reference points ρ^i for $i = 1, 2, \ldots, M$ along the tilting trajectory. For example, when $M = 4$, the reference tilting angles can be selected as $\rho^1 = 90$ deg, $\rho^2 = 60$ deg, $\rho^3 = 30$ deg, and $\rho^4 = 0$ deg. In this study, we choose $M = 20$.
(3) Calculate the nominal control input u_0^i, for example, rotor speeds, corresponding to ρ^i for $i = 1, 2, \ldots, M$, based on the nonlinear aircraft model using the Newton–Raphson search method.
(4) Linearize the nonlinear aircraft model at each tilting angle ρ^i and $[x_0^i, \dot{x}_0^i, u_0^i]$ to obtain the system matrices A^i and B^i for $i = 1, 2, \ldots, M$.
(5) Assemble the affine LPV model in the form of equation (25) with the matrix interpolations defined in equation (26).

Adaptive MPC-DRC for LPV systems

Note that $\Delta x(k+1)$ can be described by

$$\Delta x(k+1) = x(k+1) - x_0(k+1) - \dot{x}_0(k+1)T$$

hence, equation (25) can be converted into the following form

$$\Delta x(k+1) = A(\rho(k))\Delta x(k) + B(\rho(k))\Delta u(k) \tag{27}$$

Let $e(k) = \Delta x_{ref} - \Delta x(k)$ denote the tracking error at the current time step k, the adaptive MPC design[34–36] is to find the constrained optimal control law $\Delta u(k)$ over a given horizon N that minimizes the constrained quadratic performance defined by

$$\begin{aligned} \min_{\Delta u(k), \ldots, \Delta u(k+N-1)} \frac{1}{2}\Bigg\{ & e^T(k+N)Qe(k+N) \\ & + \sum_{m=0}^{N-1}\left[e^T(k+m)Qe(k+m) + \Delta u^T\right. \\ & \left.(k+m)R\Delta u(k+m)\right]\Bigg\} \text{subject to } G\Delta u \\ & (k+m) \le h, m = 0, \ldots, N-1 \end{aligned} \tag{28}$$

where $Q \ge 0$ and $R > 0$ are the weighting matrices used to penalize the tracking error $e(k)$ and control effort $\Delta u(k)$, respectively, and G a constraint matrix used to ensure that the control effort $\Delta u(k)$ stay within the prescribed bound h. In addition, $e(k+m)$ and $\Delta u(k+m)$ represent the predicted error and control input at time step m. For a finite prediction horizon of N steps, the cost function and the constraint equation in equation (28) can be rewritten in a compact form as follows

$$\min_{\widehat{u}(k)} \frac{1}{2}\left[\widehat{e}^T(k)\widehat{Q}\widehat{e}(k) + \Delta\widehat{u}^T(k)\widehat{R}\Delta\widehat{u}(k)\right] \quad \text{subject to } \widehat{G}\Delta\widehat{u}(k) \le \widehat{h} \tag{29}$$

where

$$\widehat{e}(k) = \begin{bmatrix} e(k) \\ e(k+1) \\ \vdots \\ e(k+N) \end{bmatrix} \in \mathbb{R}^{(N+1)n_x},$$

$$\Delta\widehat{u}(k) = \begin{bmatrix} \Delta u(k) \\ \Delta u(k+1) \\ \vdots \\ \Delta u(k+N-1) \end{bmatrix}, \widehat{h} = \begin{bmatrix} h \\ h \\ \vdots \\ h \end{bmatrix} \in \mathbb{R}^{Nn_u}$$

$$\widehat{R} = \begin{bmatrix} R & 0 & \dots & 0 \\ 0 & R & \dots & 0 \\ \vdots & \vdots & \ddots & \vdots \\ 0 & 0 & \dots & R \end{bmatrix}, \widehat{G} = \begin{bmatrix} G & 0 & \dots & 0 \\ 0 & G & \dots & 0 \\ \vdots & \vdots & \ddots & \vdots \\ 0 & 0 & \dots & G \end{bmatrix} \in \mathbb{R}^{Nn_u \times Nn_u},$$

$$\widehat{Q} = \begin{bmatrix} Q & 0 & \dots & 0 \\ 0 & Q & \dots & 0 \\ \vdots & \vdots & \ddots & \vdots \\ 0 & 0 & \dots & Q \end{bmatrix} \in \mathbb{R}^{(N+1)n_x \times Nn_x} \tag{30}$$

Furthermore, the predicted tracking error (over a given horizon) $\widehat{e}(k)$ can be described by

$$\widehat{e}(k) = \widehat{A}e(k) + \widehat{B}\Delta\widehat{u}(k) \tag{31}$$

where

$$\widehat{A} = [IA(\rho)A^2(\rho)\vdots A^N(\rho)] \in \mathbb{R}^{(N+1)n_x \times n_x},$$

$$\widehat{B} = \begin{bmatrix} 0 & 0 & 0 & \dots & 0 \\ B(\rho) & 0 & 0 & \dots & 0 \\ A(\rho)B(\rho) & B(\rho) & 0 & \dots & 0 \\ \vdots & \vdots & \vdots & \ddots & 0 \\ A^{N-1}(\rho)B(\rho) & A^{N-2}(\rho)B(\rho) & A^{N-3}(\rho)B(\rho) & \dots & B(\rho) \end{bmatrix} \in \mathbb{R}^{(N+1)n_x \times Nn_u}$$

As shown in equation (31), the predicted tracking error $\widehat{e}(k)$ can be determined based on the current tracking error $e(k)$ and control vector $\Delta\widehat{u}(k)$. Therefore, the optimization problem can be reformulated by utilizing the current information as follows

$$\min_{\Delta\widehat{u}(k)} \frac{1}{2}\Delta\widehat{u}^T(k)\left(\widehat{R} + \widehat{B}^T\widehat{Q}\widehat{B}\right)\Delta\widehat{u}(k) + e^T(k)\widehat{A}^T\widehat{Q}\widehat{B}\Delta\widehat{u}(k) + \frac{1}{2}e^T(k)\widehat{A}^T\widehat{Q}\widehat{A}e(k) \quad \text{subject to } \widehat{G}\Delta\widehat{u}(k) \le \widehat{h}(k) \tag{32}$$

Note that the optimal control law $\Delta\widehat{u}(k)$ obtained from the above is also the optimal solution to the constrained optimization problem defined in equations (27) and (28).

For real-time control at the current time step k, given the measured or estimated tracking error $e(k) = \Delta x_{ref} - \Delta x(k)$, the minimization problem described in equation (32) can be solved using the quadratic programming (QP) solver in Matlab.[40] Instead of applying only the first control entry $\Delta u(k + 0)$ at the current time step k and repeating the optimization process for next time step $k+1$, a control horizon of $N_c \le N$ is chosen so that the first N_c control entries $[u(k + 0), u(k + 1), \dots, u(k + N_c - 1)]$ are used between current time step k and time step $k + N_c - 1$. Subsequently, the optimization process is repeated at time step $k + N_c - 1$ to solve for the next control effort $[u(k + N_c), u(k + N_c + 1), \dots, u(k + 2N_c - 1)]$.[41]

Control input constraints

For the real-time LTI system model derived from a given tilting angle in the LPV model, an adaptive MPC law can be designed by solving equation (32) for a given set of input constraint vector h and weighting matrices Q and R. Note that these weighting matrices can be tuned to improve the performance of the closed-loop system.

It should be noted that the MPC input constraint vector h is used to capture the peak motor power, in which the motor power P for a propeller spinning at speed n is given by

$$P = C_p\rho_a n^3 D^5 \tag{33}$$

Let I_p be the propeller assembly inertia, then the propeller dynamics can be modeled as follows

$$\dot{n} = \frac{\left(-C_p\rho_a D^5 n^2 + \tau\right)}{I_p} \tag{34}$$

where τ is the propeller motor output torque and term $C_p\rho_a D^5 n^2$ denotes the resistant torque at speed n. By defining the resistant coefficient $K = C_p\rho_a D^5/I_p$ and equivalent motor driven acceleration $u = \tau/I_p$, the propeller dynamics can be rewritten as

$$\dot{n} = -Kn^2 + u \tag{35}$$

Now, consider a motor with peak power $P_{\max}$, then the maximum propeller-driven torque $\tau_{\max}$ can be computed as

$$\tau_{\max} = \frac{P_{\max}}{n} \tag{36}$$

hence, the maximum equivalent propeller acceleration $u_{\max}$ is given by

$$u_{\max} = \frac{\tau_{\max}}{I_p}$$

Substituting equation (36) into the above equation yields

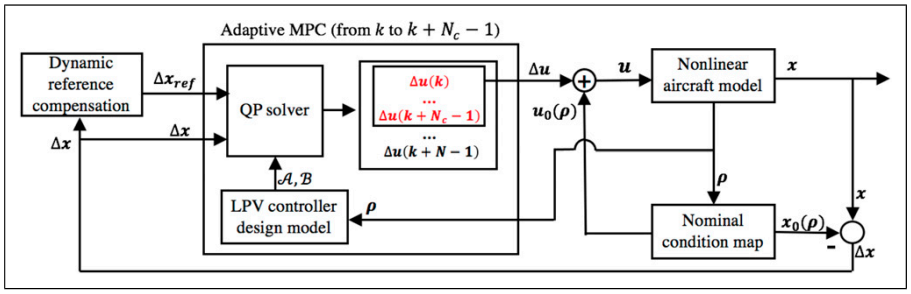

Figure 7. The proposed adaptive model predictive control-dynamic reference compensation architecture.

$$u_{\max} = \frac{P_{\max}}{I_p n} \tag{37}$$

which denotes the MPC input constraint. In summary, during the MPC design, the control input constraint $u_{\max} = f(n, P_{\max})$, and hence, constraint vector h is computed in real-time as a function of propeller speed n and motor peak power $P_{\max}$.

Dynamic reference compensation (DRC)

The proposed adaptive MPC law integrated with a feed-forward dynamic reference compensation (DRC) architecture is shown in Figure 7, where Δx and Δu denote the deviations of the controlled states and inputs as described in equation (27). In this study, the penalized tracking outputs are the forward speed Δx_2; vertical speed Δx_3 and pitch rate Δx_4; the reference vertical speed Δx_3^{ref} and reference pitch rate which are adjusted based on the relevant state status (to be discussed later) while the reference vertical speed Δx_2^{ref} is held at zero. Based on the real-time state reference signal Δx^{ref} and system state-feedback signal Δx, the adaptive MPC law generates a set of optimized control signals $\Delta u(k+m)$, $m = 0, 1, \ldots, N-1$, from which the control signals within the control horizon, that is, $[\Delta u(k) \cdots \Delta u(k+N_c-1)]$ and $N_c < N$ are selected as the optimal state-feedback control Δu and to be combined with the nominal control input $u_0(\rho)$ to form a complete control input, $u = \Delta u + u_0(\rho)$. In this study, all system states x are assumed to be measurable, and the required control feedback signal Δx is defined as $\Delta x = x - x_0(\rho)$, where $x_0(\rho)$ denotes the nominal state.

To effectively track the aircraft forward velocity during the initial transition flight Δx_4^{ref}, a dynamic reference compensation method is proposed. Since the aircraft pitch rate is directly affected by the rotor thrust forces, the forward velocity can be compensated by using a real-time reference pitch rate feedback defined by

$$\Delta x_4^{ref} = G_1(\rho)\Delta x_2$$

where Δx_2 is the forward velocity error and $G_1(\rho)$ is the sensitivity gain for dynamic reference compensation, which is a function of $\rho(t)$. As a result, to compensate for forward velocity, the MPC design assigns a small weighting on the forward velocity error $Q_{[2,2]}(\rho)$ and a large sensitivity gain $G_1(\rho)$ at the beginning of transition flight. As the transition progresses, the weighting $Q_{[2,2]}(\rho)$ increases gradually, while the sensitivity gain $G_1(\rho)$ is reduced correspondingly as the fixed-wing aerodynamic effect becomes prominent. Using the same principle, the aircraft pitch attitude control is achieved by adjusting the reference angular speed based on the feedback angular position multiplied by a tunable gain K_p. Therefore, the reference pitch rate can be given by $\Delta x_4^{ref} = G_1(\rho)\Delta x_2 - K_p\Delta x_8$. In summary, the desired forward velocity tracking can be achieved by adjusting reference pitch rate as a function of velocity error and pitch attitude, along with an increased penalty on forward velocity error depending on $\rho(t)$.

Similarly, in order to maintain altitude-hold during transition flight, reference vertical speed $\Delta x_3^{ref} = -K_v\Delta x_{12}$ is compensated using altitude error Δx_{12}, where K_v is the selected sensitivity gain. Since the middle two tilt-rotor angular position ρ can be tracked directly by regulating its acceleration $\ddot{\rho}(t)$ (or $u_{8,9}$), which is also the nominal control u_0 for the prescribed tilting trajectory. Hence, in the proposed MPC-DRC scheme, $\Delta u_{8,9}$ are constrained by $-\varepsilon \le \Delta u_{8,9} \le +\varepsilon$, where ε is chosen to allow for the tilt-rotor angle to be controlled mainly by the nominal control signal.

Simulation results

Based on the adaptive MPC-DRC framework presented in Figure 7, the MPC law is carefully calibrated to achieve the desired aircraft transition flight performance. The parameters used in the simulations are listed in Table 5, where the sensitivity gain $G_1(\rho)$ and the weight $G_2(\rho)$ are chosen to be

$$G_1(\rho) = 0.01 \times \frac{\rho}{90}, G_2(\rho) = 400^2 \times \left(1 - \frac{\rho}{90}\right), \text{for} \rho \in [90, 0]$$

As noted previously, the maximum longitudinal acceleration and the maximum tilt-rotor articulation rate are constrained by 0.189 g and 9 deg/s, respectively. In what follows, we first present the simulation results for the three articulation profiles considered in the section reference

Table 5. Adaptive MPC-DRC controller parameters.

Parameter	Value	Parameter	Value
$Q_{[2,2]}$	$G_2(\rho)$	$Q_{[3,3]}$	200^2
$Q_{[4,4]}$	4000^2	$R_{[1:6,1:6]}$	$0.01^2 \times I_6$
$R_{[9,9]}$	0.01^2	Step size, ms	1
Prediction horizon	4	Control horizon	2
min $\Delta u_{[1:6]}$	$-Kn^2_{[10:15]}$	Max $\Delta u_{[1:6]}$	$-Kn^2_{[10:15]} + \max u_{[10:15]}$
min $\Delta u_{[7,8]}$	$-\varepsilon$	Max $\Delta u_{[7,8]}$	ε
min $\Delta u_{[9]}$	-0.2	Max $\Delta u_{[9]}$	0.2
Δx_3^{ref}	$-\Delta x_{12}$	Δx_4^{ref}	$-\Delta x_8 + G_1(\rho)\Delta x_2$

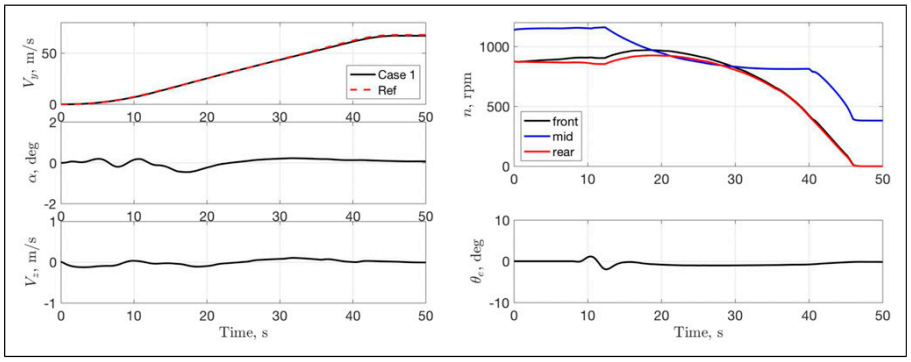

Figure 8. Controlled system responses and control efforts of normal transition—Case 1.

articulation trajectory for tilt-rotors, followed by a study of robustness of the proposed adaptive MPC-DRC architecture when the aircraft is subjected to an external disturbance during the transition flight. The first three simulation cases are designed to demonstrate the normal aircraft transition performance for the designed control strategy, where Case 1 is for the baseline transition profile (constant tilting speed), and Cases 2 and 3 are for energy-optimized profiles. The last three simulation cases are used to investigate the robustness (disturbance rejection capability) of the proposed control strategy with three different disturbances injected during the tilt transition. The simulation was conducted using Matlab 2019b with a 2.2 GHz Intel Core i7 processor, and the run-time for a 20-s simulation with the aircraft model is around 12 s. The baseline articulation profile of Case 1 is studied, where the reference trajectories $\rho(t)$ and $V_y(t)$ are given in Figure 5. The simulation results are shown in Figure 8. It can be clearly seen that the feedback-controlled system with the proposed adaptive MPC-DRC law tracks the desired longitudinal velocity V_y quite well but with small oscillations in pitch attitude α and vertical velocity V_z. These small errors are primarily caused by the fact that the LPV model is developed by interpolating a finite number of linearized models along a prescribed transition profile, leading to both modeling and nominal control ($u_0(\rho)$) errors. The corresponding control efforts, which include both the fixed-wing elevator deflection θ_c and all six rotor speeds n are also shown in Figure 8. As the tilt-rotor articulates, in order to compensate for the reduced thrust component in vertical direction and tilt-rotor thrust vector misalignment with respect to CG, the front and rear lift-rotor speeds are increased momentarily until the aircraft is able to pick up sufficient forward velocity to generate notable aerodynamic lift. Subsequently, the lift-rotors are commanded to zero speed as transition flight is complete, and only the middle tilt-rotors are regulated to ensure the aircraft maintains at the desired level flight velocity. The elevator deflection angle is clearly deflected upward ($+\theta_c$) initially to aerodynamically generate a nose-up pitching moment to assist for altitude-hold, but as the vehicle altitude is also modulated by the front and rear lift-rotor thrusts, the elevator deflection is quickly commanded to zero to pull back the pitching moment.

Based on the reference trajectories $\rho(t)$ and $V_y(t)$ showed in Figure 5, the simulation results for more aggressive tilting profile of Case 2 and the minimum energy tilting profile of Case 3 are shown in Figure 9 and Figure 10. As shown in Figure 9, the proposed adaptive MPC-DRC law enables a good tracking for longitudinal velocity V_y in both cases; however, the pitch attitude and vertical velocity oscillations are more pronounced compared to those in Case 1. This error is mainly caused by the rapid tilt-rotor articulation at the beginning of transition flight, which causes the aircraft to pitch downward initially, and hence generates downward velocity ($-V_z$). The rotor speeds and the elevator deflection angle for Cases 2 and 3 are shown in Figure 10.

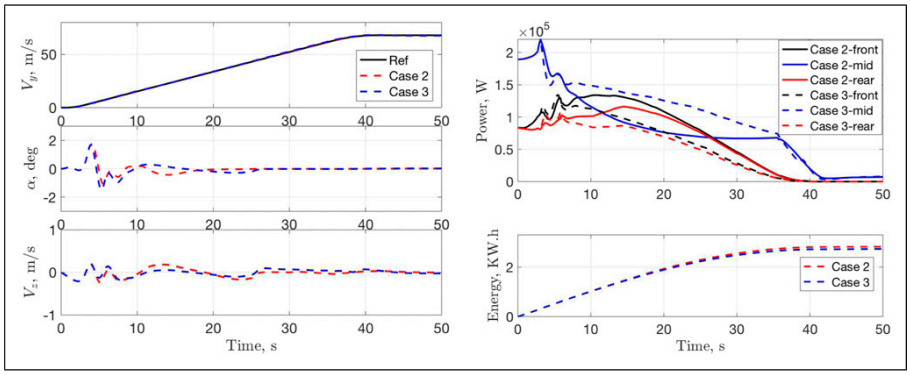

Figure 9. Simulation results of energy-optimized transition—Cases 2 and 3.

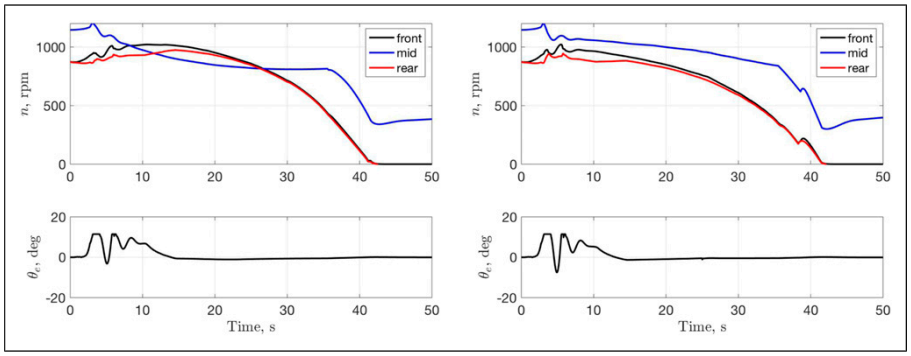

Figure 10. Control efforts of energy-optimized transition—Case 2 (left) and Case 3 (right).

Since the aircraft aggressively initiates forward velocity as tilt-rotors rapidly articulate, the elevator deflection is quickly responding to counter the pitch down moment, and the rotor speeds are all increased notably to ensure altitude-hold. As aircraft continues to pick up forward velocity, the elevator deflection is actively engaged in order to attain sufficient control authority, especially within the first 10 s or so when the aircraft is still gaining forward momentum. In addition, it can be observed in Figure 10 that the tilt-rotor speed and lift-rotor speed are better coordinated for Case 3 when compared to these results for Case 2. Figure 9 shows the comparison of power consumption of the lift-rotor and tilt-rotor, and the total energy consumption, for both Cases 2 and 3. As expected, the rotor power consumption follows the similar trends as the rotor speed observed in Figure 10, and the comparison of total energy clearly shows that Case 3 is more energy efficient, for example, at $t = 50$ s, the total energy costs for Cases 2 and 3 are 2.825 kWh and 2.735 kWh, respectively.

Next, we assess the robustness of the proposed adaptive MPC-DRC flight controllers when the aircraft is subjected to an upward disturbance during transition flight. In this preliminary analysis, we apply the disturbance to the aircraft that is following a baseline tilting profile of Case 1. The disturbance is modeled as an external vertical acceleration $d(t)$ with respect to aircraft CG as follows

$$d(t) = K\frac{1-\cos\left(\frac{2\pi t}{p}\right)}{2}$$

where K and p denote the magnitude and period of the disturbance, respectively. In this study, we assume $K = 4\ m/s^2$, and consider two cases of disturbance period p, namely Case 4 is for $p = 2$ s and Case 5 for $p = 4$ s. Furthermore, we inject one period of disturbance at 10,20,30,40 s during the transition process, and the simulation results for Cases 4 and 5 are shown in Figure 11.

As shown in Figure 11, although the disturbance-induced vertical forces F are quite substantial, the aircraft longitudinal velocity V_y is able to closely track the reference velocity trajectory in both cases. However, pitch attitude α, vertical velocity V_z, and vertical displacement D_z are notably disturbed. As the aircraft gradually gains forward velocity, the fixed-wing control surface becomes more effective; hence, the evidence of disturbance suppression capability of the proposed transition flight controllers can be clearly observed in Figure 11. In addition, the rotor speeds and elevator deflection are shown in Figure 12 for Cases 4 and 5. It can be seen that in order to counter the upward disturbance force, the rotor speeds are accordingly tuned down to reduce the vertical thrust, and the elevator is aggressively deflected downward to generate pitching-down moment,

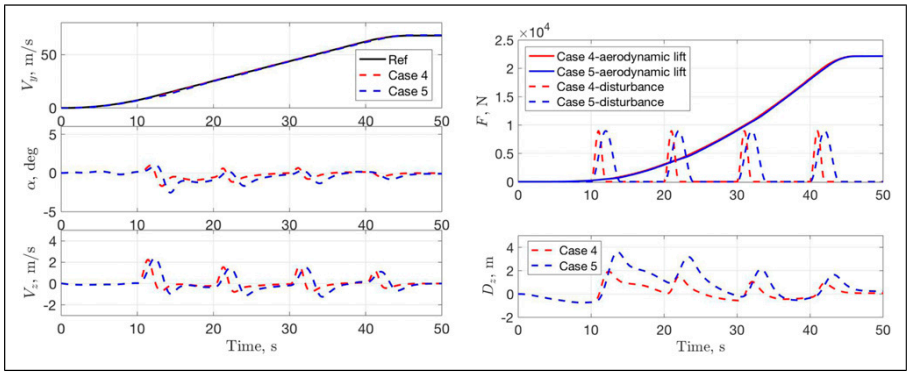

Figure 11. Simulation results of transition with disturbance—Cases 4 and 5.

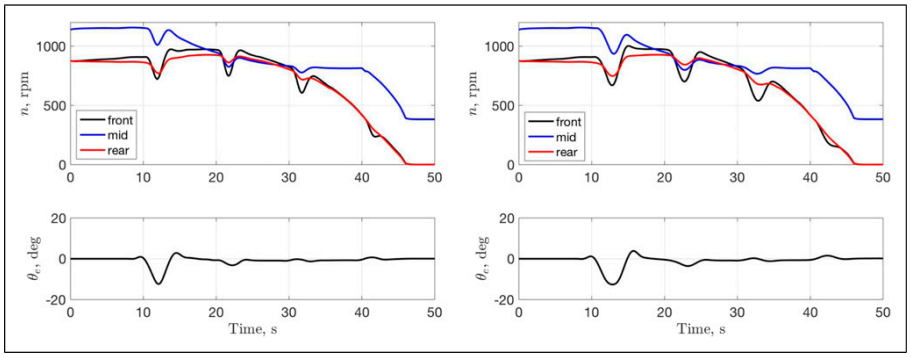

Figure 12. Control efforts of transition with disturbance—Case 4 (left) and Case 5 (right).

Table 6. Performance evaluation of simulation results.

Case	#1	#2	#3	#4	#5
RMSE of V_y	0.204 0	0.150 6	0.290 4	0.295 7	0.557 1
RMSE of V_z	0.063 0	0.093 4	0.074 8	0.486 9	0.650 9
RMSE of α	0.180 2	0.302 4	0.334 7	0.469 8	0.716 9
Total energy cost (kWh)	3.243	2.825 2	2.735 2	3.122	3.044
Peak vertical acceleration (m/s^2)	0.915 3	−0.550 1	0.453 0	−3.019 5	−2.561 4

especially during the initial disturbance injection period when the aircraft is yet to have sufficient forward velocity. The elevator and rotor speed modulations become mildly active as aircraft attained sufficient forward velocity, and they are proven to effectively reject the external disturbance.

In summary, the proposed adaptive MPC-DRC law is able to successfully achieve the transition flight by following various transition flight profiles. Table 6 summarizes the five cases studied.

Conclusion

This paper presented a study of transition flight for eVTOL aircraft configured with six distributed rotors. There are two pairs of lift-rotors located fore and aft of the aircraft CG. Only the middle two rotors that are closer to CG in the longitudinal direction are commanded to articulate. Based on the nonlinear aircraft model developed earlier, a simplified force analysis model was introduced and used to develop various reference transition flight profiles. In particular, a tilt-rotor articulation profile that requires the minimum energy was derived by formulating the power-driven transition problem as a problem of energy optimization problem. A set of linearized models was obtained along the prescribed transition profile; in addition, based on the nonlinear rigid-body aircraft model, an affine LPV model was constructed so that a linear model can be attained by interpolating its neighboring linearized models. A novel transition flight control concept was proposed that combines the adaptive MPC with the dynamic reference compensation (DRC) to enable feedback-feedforward control capability, and it was successfully used for controlling transition flights subjected to constant as well as

time-varying design constraints. The simulation results demonstrated the efficacy of the proposed adaptive MPC-DRC transition flight control by analyzing nominal tilt-rotor articulation profiles. To demonstrate the robustness of the proposed concept, additional simulations were conducted by injecting the disturbance into the aircraft during its transition flight. These simulations also showed favorable disturbance rejection capability of the proposed transition flight control. The future research will include the study of rotor failure during transition flight.

Declaration of Conflicting Interests

The author(s) declared no potential conflicts of interest with respect to the research, authorship, and/or publication of this article.

Funding

The author(s) received no financial support for the research, authorship, and/or publication of this article.

ORCID iDs

Guoming Zhu https://orcid.org/0000-0002-2101-2698
Weihua Su https://orcid.org/0000-0002-4458-0524

References

1. Holden J and Goel N. *Uber elevate: fast-forwarding to a future of on-demand Urban air transportation*. 2016. https://evtol.news/__media/PDFs/UberElevateWhitePaperOct2016.pdf
2. Binder R, Garrow L, German B, et al. If you fly it, will commuters come? Predicting demand for evtol urban air trips. In: AIAA Conference, Atlanta, Georgia, 2018: 1–41.
3. Dorrington GE, et al. Performance of electric vertical take-off and landing (EVTOL) hovering craft. In: AIAC18: 18th Australian International Aerospace Congress (2019): HUMS-11th Defence Science and Technology (DST) International Conference on Health and Usage Monitoring (HUMS 2019): ISSFD-27th International Symposium on Space Flight Dynamics (ISSFD), Engineers Australia, Royal Aeronautical Society, Australia, Melbourne, 1 January 2019: 84.
4. Kleinbekman IC, Mitici MA and Wei P. eVTOL arrival sequencing and scheduling for on-demand Urban air mobility. In: 2018 IEEE/AIAA 37th Digital Avionics Systems Conference (DASC), London, UK, 23–27 September 2018. IEEE: 1–7.
5. German B, Daskilewicz M, Hamilton TK, et al. Cargo delivery in by passenger eVTOL aircraft: a case study in the san francisco bay area. *2018 AIAA Aerospace Sciences Meeting*, Kissimmee, Florida, 8–12 January 2018. DOI: 10.2514/6.2018-2006.
6. Pradeep P and Wei P. *Heuristic approach for arrival sequencing and scheduling for eVTOL aircraft in on-demand Urban air mobility*. In: 2018 IEEE/AIAA 37th Digital Avionics Systems Conference (DASC). IEEE: 1–7.
7. Skuhersky M. *A first-principle power and energy model for eVTOL vehicles*. MS thesis, Melbourne, Florida, USA: Florida Institute of Technology, 2019.
8. Pradeep P and Wei P. "Energy efficient arrival with RTA constraint for urban eVTOL operations,". *2018 AIAA Aerosp Sci Meet* 2018; 1–13.
9. Daskilewicz M, German B, Warren M, et al. Progress in vertiport placement and estimating aircraft range requirements for eVTOL Daily Commuting. In: 2018 Aviation Technology, Integration, Operations Conference, Atlanta, Georgia, 25-29 June 2018: 2884.
10. Payuhavorakulchai P. *Cost analysis of EVTOL configuration design for air ambulance in Japan. Master's Dissertation*. Tokyo, Japan: Minato CityKeio University, 2019.
11. Vegh JM, Botero E, Clarke M, et al. Current capabilities and challenges of NDARC and SUAVE for eVTOL aircraft design and analysis. In: AIAA Propulsion and Energy 2019 Forum, Reston, Virginia, 2019: 1–15.
12. Boddupalli SS. *Estimating demand for an electric vertical landing and takeoff (eVTOL) air taxi service using discrete choice modeling. PhD thesis*. Atlanta, Georgia, USA: Georgia Institute of Technology, 2019.
13. Lombaerts T, Kaneshige J, Schuet S, et al. Nonlinear dynamic inversion based attitude control for a hovering quad tiltrotor eVTOL vehicle. *AIAA Scitech 2019 Forum*, San Diego, California, 7-11 January 2019: 0134.
14. Basset P-M, Vu BD, Beaumier P, et al. Models and methods at ONERA for the presizing of eVTOL hybrid aircraft including analysis of failure scenarios. In: AHS International 74th Annual Forum & Technology Display, Phoenix, Arizona, USA, 14-17 May 2018.
15. Lombaerts T, Kaneshige J, Schuet S, et al. Dynamic inversion based full envelope flight control for an eVTOL vehicle using a unified framework. In: AIAA Scitech 2020 Forum, Orlando, FL, 6-10 January 2020: 1619.
16. Chauhan SS and Martins JR. Tilt-wing eVTOL takeoff trajectory optimization. *J Aircraft* 2020; 57(1): 93–112.
17. Mehra RK, Prasanth RK and Gopalaswamy S. XV-15 tiltrotor flight control system design using model predictive control. In: 1998 IEEE Aerospace Conference, Snowmass, CO, 28-28 March 1998.
18. Zhang J, Liguo S, Xiangju Q, et al. Time-varying linear control for tiltrotor aircraft. *Chinese J Aeronautics* 2018; 31(4): 632–642.
19. Rysdyk RT and Calise AJ. Adaptive model inversion flight control for tilt-rotor aircraft. *J Guidance, Control, Dynamics* 1999; 22(3): 402–407.
20. Lyu Z, Wang Z, Duan D, et al. Tilting path optimization of tilt quad rotor in conversion process based on ant colony optimization algorithm. *IEEE Access* 2020; 8: 140777–140791.
21. Gao J, Zhang Q, Chen J, et al. Take-off trajectory optimization of tilt-rotor aircraft based on direct allocation method. *IOP Conf Ser Mater Sci Eng* 2020; 768: 042004.IOP Publishing.
22. Wang X and Cai L. Mathematical modeling and control of a tilt-rotor aircraft. *Aerosp Sci Technol* 2015; 47: 473–492.
23. Cetinsoy E, Dikyar S, Hançer C, et al. Design and construction of a novel quad tilt-wing UAV. *Mechatronics* 2012; 22(6): 723–745.
24. Su W, Qu S, Zhu GG, et al. A control-oriented dynamic model of tiltrotor aircraft for urban air mobility. In: AIAA Scitech 2021 Forum, virtual event, 11–15 & 19–21 January 2021: 0091.
25. Shamma JS. *An overview of LPV systems," control of linear parameter varying systems with applications*. Boston, MA, USA: Springer, 2012, pp. 3–26.
26. Qu S, He T and Zhu GG. Engine EGR valve modeling and switched LPV control considering nonlinear dry friction. *IEEE/ASME Trans Mechatronics* 2020; 25: 1668–1678.

27. Qu S, He T and Zhu GG. *LPV modeling and switched control for EGR valves with dry friction*. 2019 IEEE Conference on Control Technology and Applications (CCTA). IEEE, 2019, pp. 400–405.
28. He T, Zhu GG, Swei SS-M, et al. Smooth-switching LPV control for vibration suppression of a flexible airplane wing. *Aerosp Sci Technol* 2019; 84: 895–903.
29. He T, Al-Jiboory AK, Zhu GG, et al. Application of ICC LPV control to a blended-wing-body airplane with guaranteed H∞ performance. *Aerosp Sci Technol* 2018; 81: 88–98.
30. Fukushima H, Kim T-H and Sugie T. Adaptive model predictive control for a class of constrained linear systems based on the comparison model. *Automatica* 2007; 43(2): 301–308.
31. Kim J-S. Recent advances in adaptive MPC. In: ICCAS 2010, Gyeonggi-do, Korea (South), 27-30 October 2010. IEEE: 218–222.
32. Ding B. *Dynamic output feedback MPC for LPV systems via near-optimal solutions*. In: Proceedings of the 30th Chinese Control Conference, Yantai, China, 2011: IEEE: 3340–3345.
33. Casavola A, Famularo D and Franze G. A feedback min-max MPC algorithm for LPV systems subject to bounded rates of change of parameters. *IEEE Trans Automatic Control* 2002; 47(7): 1147–1153.
34. Camacho EF and Alba CB. *Model predictive control*. 2nd ed.. London, UK: Springer Science & Business Media, 2013.
35. Mayne DQ, Rawlings JB, Rao CV, et al. Constrained model predictive control: Stability and optimality. *Automatica* 2000; 36(6): 789–814.
36. Garcia CE, Prett DM and Morari M. Model predictive control: theory and practice—a survey. *Automatica* 1989; 25(3): 335–348.
37. Anderson JD. *Aircraft performance and design*. New York, NY, USA: McGraw-Hill Education, 1998.
38. Wang C, Zhao X, Fu R, et al. Research on the comfort of vehicle passengers considering the vehicle motion state and passenger physiological characteristics: improving the passenger comfort of autonomous vehicles. *Int J Environ Res Public Health* 2020; 17(18): 6821.
39. Al-Jiboory AK, Zhu G, Swei SS-M, et al. LPV modeling of a flexible wing aircraft using modal alignment and adaptive gridding methods. *Aerospace Science Technology* 2017; 66: 92–102.
40. Schmid C and Biegler LT. Quadratic programming methods for reduced Hessian SQP. *Comput Chemical Eng* 1994; 18(9): 817–832.
41. Phuong TH, Belov MP and Van Thuy D. Adaptive model predictive control for nonlinear elastic electrical transmission servo drives. In: 2019 IEEE Conference of Russian Young Researchers in Electrical and Electronic Engineering (EIConRus), Saint Petersburg and Moscow, Russia, 28–31 January 2019. IEEE, 2019: 704–708.